Physica Scripta

PAPER • **OPEN ACCESS**

High-power diode lasers with *in-situ*-structured lateral current blocking for improved threshold, efficiency and brightness

To cite this article: M Elattar *et al* 2023 *Phys. Scr.* **98** 015506

View the article online for updates and enhancements.

You may also like

- Analysis on light power and three-dimentional temperature distribution characteristics of gain guided and index alternate-guided fiber lasers
Xiao Shen, Liaolin Zhang, Jianyong Ding et al.

- On carbon transport and fate in the East Siberian Arctic land–shelf–atmosphere system
Igor P Semiletov, Natalia E Shakhova, Valentin I Sergienko et al.

- Gain and index guiding in a Raman generator with diffraction-free pump beams
R V Chulkov, P A Apanasevich and V A Orlovich

This content was downloaded from IP address 89.245.22.220 on 10/02/2023 at 06:02

Physica Scripta

OPEN ACCESS

RECEIVED
5 September 2022

REVISED
24 November 2022

ACCEPTED FOR PUBLICATION
25 November 2022

PUBLISHED
8 December 2022

Original content from this work may be used under the terms of the Creative Commons Attribution 4.0 licence.

Any further distribution of this work must maintain attribution to the author(s) and the title of the work, journal citation and DOI.

PAPER

High-power diode lasers with *in-situ*-structured lateral current blocking for improved threshold, efficiency and brightness

M Elattar, O Brox, P Della Casa, A Mogilatenko, A Maaßdorf, D Martin, H Wenzel, A Knigge, M Weyers and P Crump

Ferdinand-Braun-Institut (FBH), Gustav-Kirchhoff-Str. 4, 12489 Berlin, Germany

E-mail: mohamed.elattar@fbh-berlin.de

Keywords: broad-area diode laser, high power, self-aligned, epitaxial regrowth, *in situ* etching, current blocking, lateral current confinement

Abstract

We present high-power GaAs-based broad-area diode lasers with a novel variant of the enhanced self-aligned lateral structure 'eSAS', having a strongly reduced lasing threshold and improved peak conversion efficiency and beam quality in comparison to their standard gain-guided counterparts. To realize this new variant (eSAS-V2), a two-step epitaxial growth process involving *in situ* etching is used to integrate current-blocking layers, optimized for tunnel current suppression, within the p-$Al_{0.8}GaAs$ cladding layer of an extreme-triple-asymmetric epitaxial structure with a thin p-side waveguide. The blocking layers are thus in close proximity to the active zone, resulting in strong suppression of current spreading and lateral carrier accumulation. eSAS-V2 devices with 4 mm resonator length and varying stripe widths are characterized and compared to previous eSAS variant (eSAS-V1) as well as gain-guided reference devices, all having the same dimensions and epitaxial structure. Measurement results show that the new eSAS-V2 variant eliminates an estimated 89% of lateral current spreading, resulting in a strong threshold current reduction of 29% at 90 μm stripe width, while slope and series resistance are broadly unchanged. The novel eSAS-V2 devices also maintain high conversion efficiency up to high continuous-wave optical power, with an exemplary 90 μm device having 51.5% at 20 W. Near-field width is significantly narrowed in both eSAS variants, but eSAS-V2 exhibits a wider far-field angle, consistent with the presence of index guiding. Nonetheless, eSAS-V2 achieves higher beam quality and lateral brightness than gain-guided reference devices, but the index guiding in this realization prevents it from surpassing eSAS-V1. Overall, the different performance benefits of the eSAS approach are clearly demonstrated.

1. Introduction

Owing to their higher power conversion efficiency compared to all other light sources, the demand for high-power GaAs-based broad-area diode lasers (BALs) remains high in a wide array of applications. They are heavily utilized in material processing applications (directly or as pump sources for solid-state lasers), which demand BALs with ever-higher efficiency and beam quality. Power conversion efficiency is defined as $\eta_E = P_{opt}/(I \cdot U)$, where P_{opt}, I and U correspond to the output optical power and the operating current and voltage, respectively. The vertical beam quality is typically very high in BALs, as the output beam exhibits an almost diffraction-limited profile along the vertical axis. Progress in BAL beam quality is therefore typically quantified along the lateral axis in terms of brightness (B_{lat}) and beam parameter product (BPP_{lat}), where $B_{lat} = P_{opt}/BPP_{lat}$, and $BPP_{lat} = 0.25 \times W_{95\%} \times \theta_{95\%}$, with $W_{95\%}$ and $\theta_{95\%}$ being the near-field width and far-field angle containing 95% of the optical power. To sum up, it remains crucial to further improve BAL performance, to enable novel applications and reduce costs for existing ones. This can be achieved by studying and addressing different limitations to their performance, aiming to obtain higher P_{opt}, η_E, and B_{lat} (i.e. lower BPP_{lat}).

Many of the limitations to BAL performance are related to thermal mechanisms connected with the increase in active-zone temperature (ΔT_{AZ}) with increasing current, which occurs as a result of non-ideal power

© 2022 The Author(s). Published by IOP Publishing Ltd

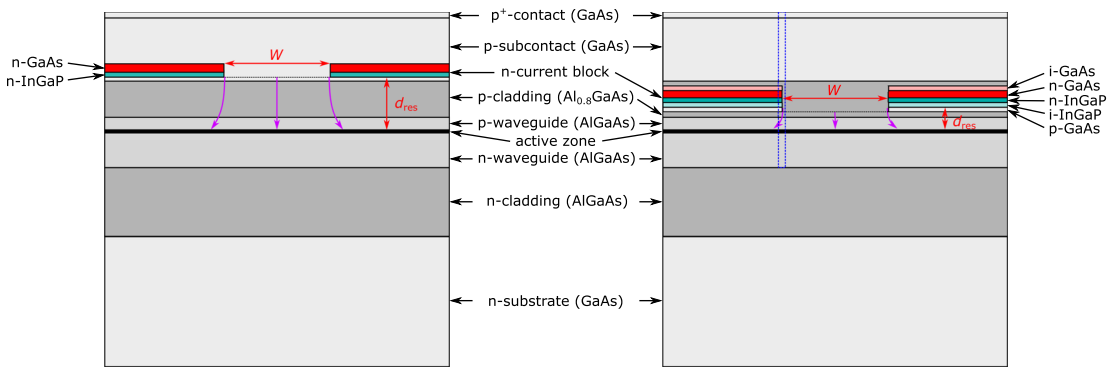

Figure 1. Schematic transverse cross sections of broad-area diode lasers with two variants of the enhanced self-aligned lateral structure (eSAS): (left) eSAS-V1 with current-blocking layers near the bottom of the p-GaAs subcontact layer, and (right) eSAS-V2 with blocking layers within the p-$Al_{0.8}GaAs$ cladding layer. The stripe width (W), residual thickness (d_{res}), and lateral current spreading are indicated.

conversion ($\eta_E < 100\%$) and heat extraction (thermal resistance $R_{th} > 0$). These mechanisms include thermal lensing, which leads to thermal far-field blooming (higher $\theta_{95\%}$) and thus higher BPP_{lat} [1, 2], as well as thermal roll-over, which reduces η_E at high current levels and limits the maximum P_{opt} [3]. However, there are also several non-thermal mechanisms that have been demonstrated via simulation and measurement results to significantly limit BAL performance. These include lateral current spreading, which introduces losses outside the BAL stripe, resulting in lower differential quantum efficiency [4, 5] and higher threshold current (I_{th}) [6]. Another non-thermal mechanism is lateral charge-carrier accumulation (LCA) at stripe edges, which increases modal gain for higher-order lateral modes with higher $W_{95\%}$ and $\theta_{95\%}$, leading to non-thermal far-field blooming and an overall higher BPP_{lat} [7–9].

The detrimental effects of current spreading and LCA can be reduced by altering the lateral structure, such that current and carriers are centrally confined under the laser stripe. To this end, a variety of lateral structuring techniques have been implemented, which we have reviewed in a previous work [10]. It remains challenging, however, to optimize the lateral design for highest B_{lat}, because modifications to reduce BPP_{lat} tend to compromise P_{opt} and η_E, for example by introducing optical losses. However, we have recently developed and presented a novel lateral structuring technique, which achieves strong current and carrier confinement and enhanced beam quality with no power or efficiency loss, namely the enhanced self-aligned lateral structure (eSAS) [10–12], shown in figure 1.

In this work, we present the development of an improved eSAS variant with even stronger lateral confinement. The paper is structured as follows: In section 2, we discuss the eSAS in detail and present the design steps and simulation results for the new eSAS BALs, then in section 3, we demonstrate a first realization of these devices and test the quality of various process aspects, using transmission electron microscopy (TEM) among other methods. Finally, in section 4, we compare the performance of the two variants of eSAS BALs to comparable reference devices, and provide a detailed analysis of the results.

2. Device design and simulation results

The enhanced self-aligned structure (eSAS) uses two-step epitaxial growth with an intermediate etching step to introduce structured n-doped layers within the p-doped side of the BAL, that are selectively etched in the device center. This creates a p-n-p configuration outside the center, which blocks current due to the reverse-biased p–n-junction. Current and carriers are thus confined to this central aperture, thereby defining a laser stripe with width W, as shown in figure 1. As explained in [10, 11], the eSAS is an enhanced variant of the self-aligned structure (SAS) [13–15], with two main improvements. First, two n-doped blocking layers (GaAs on top of InGaP) are used, compared to one GaAs layer in established SAS realizations. This enables the use of selective etching for higher etch depth precision and thus higher process control and repeatability, in addition to improving current blocking due to InGaP having a wider band gap than GaAs. Second, the eSAS is realized within an extreme-triple-asymmetric (ETAS) epitaxial structure with very thin p-side waveguide and cladding layers (combined thickness <800 nm) [3, 16], designed to have the fundamental optical mode strongly shifted to the n-side (see figure 2). This means that the blocking layers could be grown closer to the active zone (i.e. smaller residual thickness d_{res}) than in previous SAS realizations, without affecting the fundamental mode or altering its effective refractive index ($n_{eff,0}$) in the outer blocking regions. Otherwise, the resulting difference in $n_{eff,0}$ between the central and outer regions ($\Delta n_{eff,0}$) would represent undesired additional lateral index guiding that

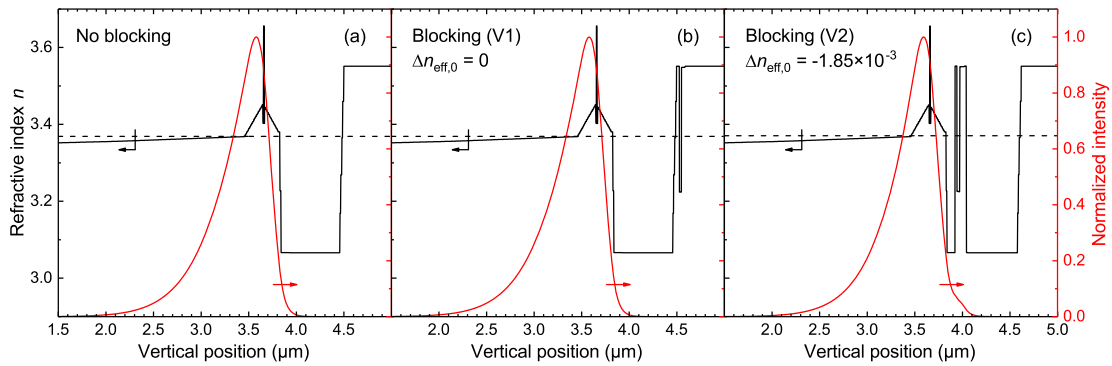

Figure 2. Refractive index and normalized optical intensity of the fundamental vertical mode as functions of vertical position along the layer structure of an eSAS BAL in: (a) the central aperture with no current blocking, (b) outer blocking region of the V1 configuration, and (c) outer blocking region of the V2 configuration. The effective refractive index ($n_{eff,0}$) of the mode is indicated by a dashed horizontal line in each case, and the differences in $n_{eff,0}$ between the non-blocking and blocking regions ($\Delta n_{eff,0}$) are indicated in the legends.

could lead to reduced beam quality [17]. The ETAS structure also enables highly efficient BAL performance up to high current levels, by combining the thin p-side waveguide and cladding layers with high optical confinement and modal gain. The thin layers ensure low series resistance, optical absorption and carrier leakage, while the high modal gain reduces I_{th} and thermal power saturation, thus resulting in high η_E at high P_{opt} [3]. The ETAS variant used here is the same as in [10], having a confinement factor $\Gamma \approx 1\%$ and internal optical loss $\alpha_i \approx 0.5\ \mathrm{cm}^{-1}$.

In the first variant (V1) of eSAS BALs, shown in figure 1(left), the blocking layers were located near the bottom of the p-GaAs subcontact layer, with d_{res} in the 800–900 nm range. Using a waveguide equation solver ('QIP2' [18]), we determined that this configuration does not induce lateral waveguiding ($\Delta n_{eff,0} = 0$; see figure 2(b) versus (a)). We have previously realized and presented the eSAS-V1 design [10–12], demonstrating clear performance advantages over gain-guided reference devices in terms of BPP_{lat}, I_{th} and peak η_E ($\eta_{E,peak}$), with no series resistance penalty or reduction in polarization purity.

It is thus appealing to develop a new configuration with smaller d_{res}, i.e. with blocking layers within the p-AlGaAs layers closer to the active zone, aiming to obtain stronger current and carrier confinement and increase the benefits of the eSAS approach. However, this inevitably adds process complexity, because aluminium oxidizes rapidly which means that performance would strongly deteriorate if AlGaAs layers are exposed to air between the two epitaxial growth steps. This is especially true in the ETAS variant used here, where the cladding layer has high aluminium content (80%). Therefore, it becomes necessary to introduce an *in situ* etching step, i.e. etching inside the metalorganic vapour-phase epitaxy (MOVPE) reactor, as performed e.g. in [19].

In this work, we have developed a second variant (V2) of eSAS BALs with blocking layers within the p-$Al_{0.8}GaAs$ cladding layer, and implemented such an *in situ*-etching approach to successfully realize it, as shown in figure 1(right). The V2 blocking structure consists of two n-doped blocking layers (GaAs on top of InGaP), just like V1. However, a thin undoped layer is added on each side of the blocking layers, thus creating a p-i-n-i-p configuration. Moreover, the n-doping concentration of the blocking layers is significantly reduced, but blocking capability is not compromised because the added undoped thickness counteracts the reduced doping. The aim of these modifications, namely the undoped layers and reduced n-doping, is to widen the depletion regions of the p–n-junctions in order to weaken the electric field across them and reduce the probability of inter-band tunneling, thus enhancing the overall current-blocking capability [20, 21]. In addition, a thin p-doped GaAs layer is added at the bottom of the blocking structure, which is necessary for the aforementioned *in situ* etching. The process of realizing eSAS-V2 devices is as follows: the first growth step stops after growing the blocking structure (with additional sacrificial layers on top) and the wafers are taken out of the reactor, where the undoped and n-doped blocking layers are laterally structured by selectively etching them in the center using wet chemical etching. With the p-GaAs layer exposed in the center, the wafers are placed back into the reactor, where CBr_4 is used for *in situ* etching of the p-GaAs layer in the central stripe and the sacrificial layers outside the stripe, followed by epitaxial regrowth of the rest of the vertical structure. In this way, a continuous p-$Al_{0.8}GaAs$ cladding is realized in the central stripe region, with no exposure to air.

The eSAS-V2 configuration presented here has a d_{res} in the 200–300 nm range. The QIP2 simulation estimates $\Delta n_{eff,0} \approx -1.85 \times 10^{-3}$ for this configuration, i.e. significant lateral index anti-guiding, due to the blocking structure layers (GaAs and InGaP) having higher refractive indices than the surrounding $Al_{0.8}GaAs$ and

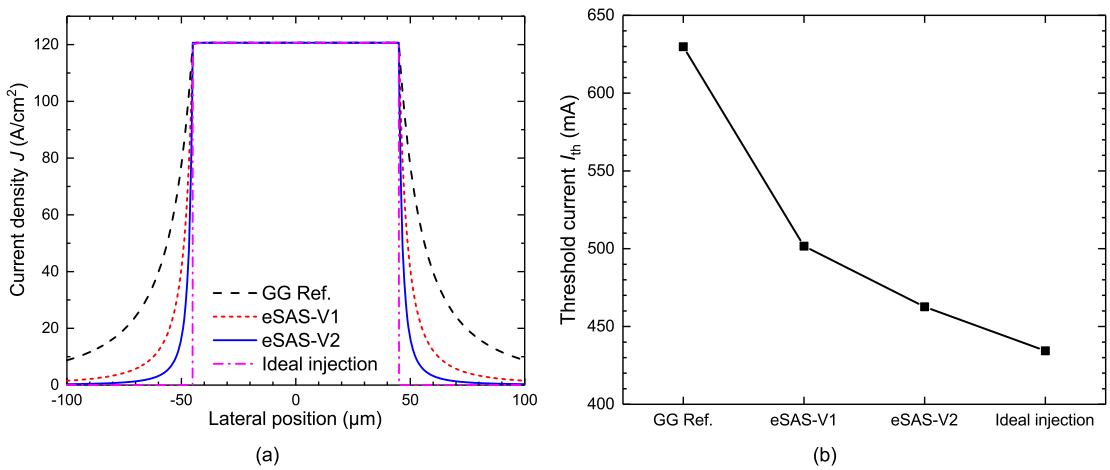

Figure 3. Simulation results (based on [24, 25]) comparing the impact of lateral current spreading in the eSAS variants (V1 and V2) and a gain-guided reference (no confinement) to the ideal injection case (no spreading), in terms of: (a) current density at threshold as a function of lateral position within the active zone, and (b) threshold current (I_{th}).

spatially overlapping with the vertical mode profile in the outer region (see figure 2(c) versus (a)). On the other hand, it has been demonstrated via simulation and measurement results that the thermally-induced lateral index guide (thermal lensing) has a value in the $+10^{-3}$ range at optical powers close to the operating point [22, 23]. Since the two opposing waveguiding mechanisms are on the same order of magnitude, we anticipate that they should counteract each other.

As previously described in [10], we can use the analytical model from [24, 25] to estimate the impact of the eSAS designs on reducing lateral current spreading, thereby reducing I_{th}. In figure 3(a), the model is used to simulate the lateral current density profiles at threshold using different device configurations, where the threshold current density (J_{th}) is calculated following [3], and they are compared to an ideal injection profile with no current spreading. It is clear from the figure that the eSAS-V2 configuration is more effective at reducing current spreading than V1, and closer to the ideal injection case. From these current density profiles, I_{th} can then be calculated, as shown in figure 3(b). Relative to the ideal injection case, the eSAS-V2 design has a 6.5% higher I_{th}, compared to 15.5% and 45.0% for the eSAS-V1 and reference designs, respectively. This corresponds to a reduction of current loss in the device edges by 85.5% for the V2 design and 65.5% for the V1 design, relative to the gain-guided reference.

3. Design realization and quality control

3.1. Oxygen incorporation test using secondary ion mass spectrometry

Before realizing eSAS-V2 BALs, simpler test devices are first processed, to test the effectiveness of the proposed process with the additional *in situ* etching step (see section 2) in preventing Al oxidation within the p-$Al_{0.8}GaAs$ cladding. In this simpler process, after the first growth step, non-selective etching of the blocking layers (*ex-situ*) and the underlying p-GaAs layer (*in situ*) takes place, followed by regrowth, which results in test devices with no lateral structuring. Oxygen content along the vertical structure is then measured using secondary ion mass spectrometry (SIMS), as shown in figure 4(a), with the measured Al content also plotted for orientation. An oxygen peak is observed at the etch-regrowth interface, but with very low concentration ($<4 \times 10^{16}$ cm^{-3}). This result demonstrates that using the proposed eSAS-V2 process, the p-i-n-i-p blocking structure can be successfully integrated within the p-$Al_{0.8}GaAs$ cladding in close proximity to the active zone, while minimizing Al oxidation and the subsequent performance deterioration.

3.2. Current blocking test

For the first realization of eSAS-V2 BALs, the epitaxial growth and wafer processing are carried out as described in section 2. In order to test the current-blocking capability of the V2 blocking structure with a p-i-n-i-p layer sequence within the p-$Al_{0.8}GaAs$ cladding layer, we process current-blocking test devices alongside BALs by excluding them from the selective etching step between the two growth steps. These test devices thus have no current aperture and do not operate as lasers due to very low current flow, but their current-voltage (I-U) characteristics can be used to evaluate the effectiveness of the blocking structure [10, 11]. The I-U characteristics are measured using two probe needles; one connected to a source-measure unit (SMU) to apply voltage and

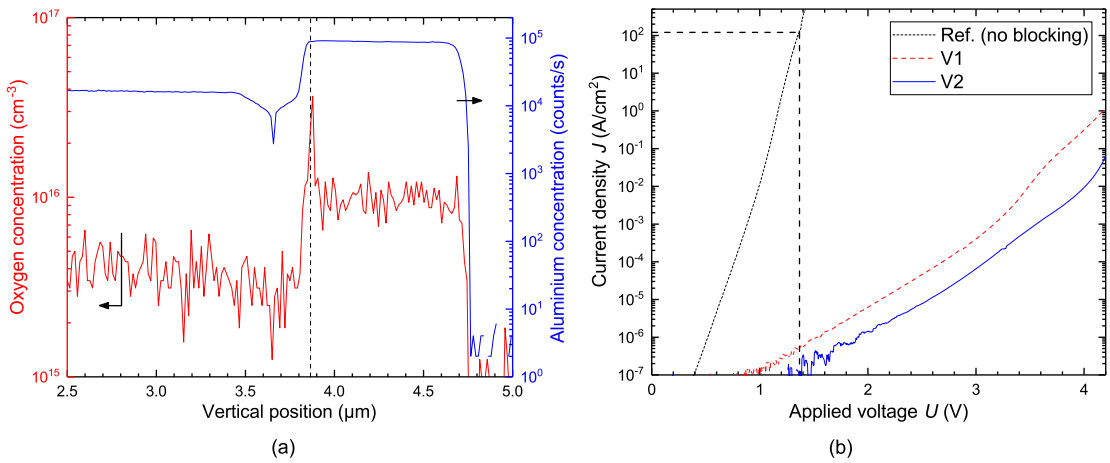

Figure 4. (a) Oxygen and aluminium concentrations as functions of vertical position along an unstructured V2 test device, measured using secondary ion mass spectrometry (SIMS), with the etch-regrowth interface indicated by a dashed line, and (b) measured current density as a function of applied voltage for V1 and V2 current-blocking test devices as well as a reference (non-blocking) BAL, all having the same dimensions. The threshold current density (J_{th}) and the corresponding bias voltage in the reference BAL (U_{th}) are also indicated.

measure current, and the other connected to a multimeter to form a four-point probe and provide an accurate voltage reading across the device. For comparison, a V1 current-blocking test device (with a p-n-p layer sequence within the p-GaAs subcontact layer) and a reference non-blocking BAL are also measured using the same technique, with the 3 devices having the same dimensions (90 μm width and 2 mm length).

The measurement results are shown in figure 4(b), showing very effective current blocking in both blocking test devices. As indicated on the figure, we compare current density (J) levels at the bias voltage (U_{th}) corresponding to J_{th} in the reference device, to quantify current-blocking capability within the standard operating voltage range of BALs. We observe that at $U_{th} \approx 1.36$ V, current density in the V1 and V2 blocking devices is 8–9 orders of magnitude lower than J_{th}, demonstrating very strong current blocking that keeps them significantly below threshold up to voltages much higher than the BAL operating voltage range. At 4.2 V, the V1 structure exhibits $J \approx 1.2$ A/cm^2 (1% of J_{th}), while the V2 structure exhibits $J \approx 0.06$ A/cm^2 (0.05% of J_{th}). Comparing the blocking structures to each other, we observe that the V2 p-i-n-i-p structure blocks current more effectively than its V1 p-n-p counterpart across the whole applied voltage range. It's important to note that the thin undoped layers add to the total thickness of the p-i-n-i-p structure, which inherently improves current blocking, but as mentioned in section 2, this effect is counteracted by a significant reduction in the doping concentration of the n-doped layers. In addition, the differences in the composition and doping concentration of the surrounding p-doped layers in each case also have an inherent impact on the current-blocking capability. Although the comparison is non-ideal, this result is nonetheless consistent with the expectation that p-i-n-i-p structures enhance current blocking relative to p-n-p structures by reducing the probability of inter-band tunneling, as discussed in section 2.

3.3. Structural quality analysis using transmission electron microscopy

Before proceeding to optoelectronic characterization, transmission electron microscopy (TEM) imaging is carried out to analyze the structural quality of eSAS-V2 BALs in their first realization. Figure 5 shows scanning TEM (STEM) images of the edge of a representative central current aperture. In figure 5(a), the high-angle annular dark-field (HAADF) imaging method is used, which exhibits a contrast strongly dependent on the mean atomic number (Z-contrast) and the local thickness of the TEM specimen, whereas figure 5(b) uses the annular dark-field (ADF) method, which predominantly exhibits strain contrast, allowing the analysis of crystal defect distribution within the heterostructure. Upon epitaxial regrowth over the laterally structured blocking layers, the inclined sidewalls of the aperture experience a different growth rate compared to planar parts of the surface. This leads to the formation of non-planar growth fronts, which are clearly visible in figure 5(a). After regrowth of the $Al_{0.8}GaAs$ cladding, the local height difference at the aperture edge is larger than the total thickness of the blocking layers, due to the different growth rates, but the subsequent regrowth of the GaAs contact layer significantly flattens the surface. Depending on the applied growth parameters, 3-dimensional AlGaAs regrowth can lead to self-organization of aluminium within the layers, resulting in Al-rich and Al-poor regions [26]. To determine if this effect occurs here, we use HAADF STEM imaging in combination with energy-dispersive x-ray spectroscopy (EDXS). Using these techniques, no change in Al content is observed above the aperture edges, indicating an inhomogeneity lower than 1 atomic percent.

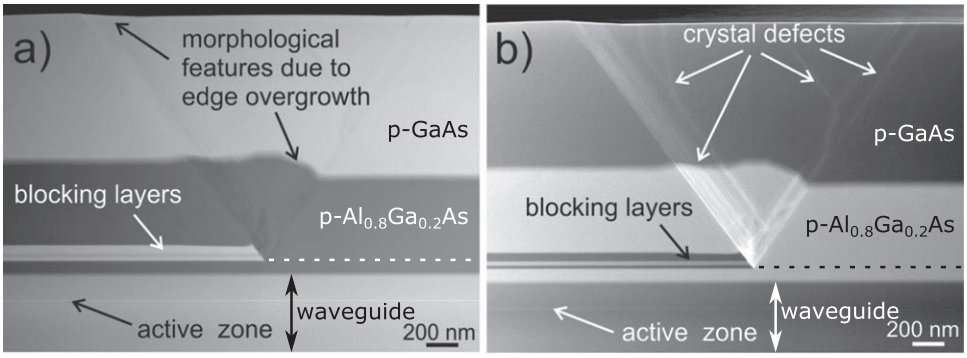

Figure 5. STEM images showing typical structural features resulting from epitaxial regrowth over the edge of an eSAS-V2 BAL aperture, using the (a) HAADF and (b) ADF imaging methods. The imaged area is roughly outlined with a dashed blue rectangle on the device schematic in figure 1(right).

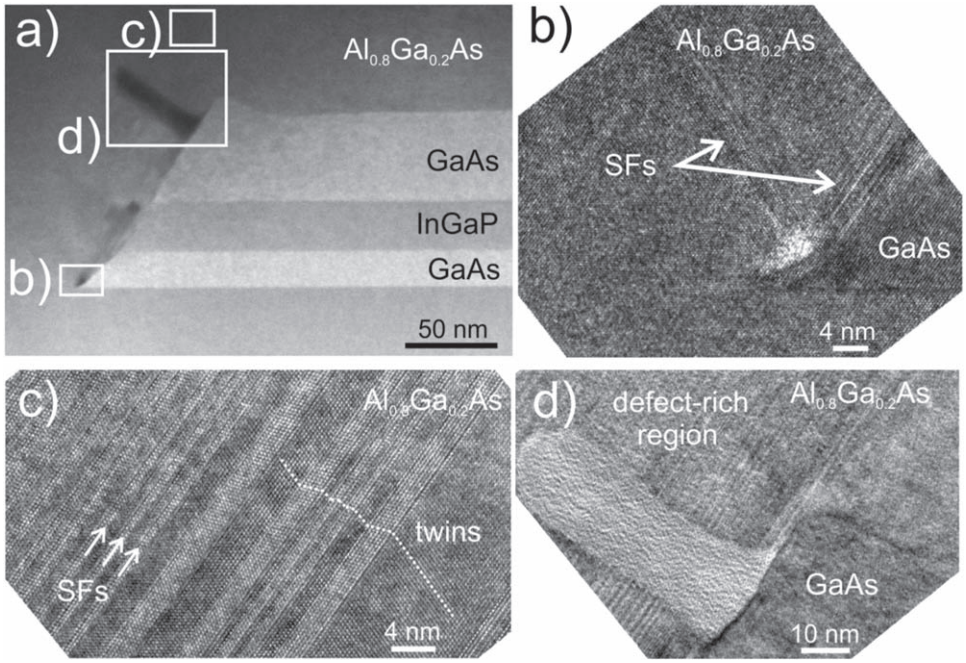

Figure 6. (a) HAADF STEM image of the edge of an eSAS-V2 BAL aperture, (b), (c) and (d) HRTEM images of specific areas indicated on (a), demonstrating the formation of stacking faults (SFs), twins and voids as a result of the epitaxial regrowth of $Al_{0.8}GaAs$ over the aperture edge.

However, as shown in figures 5(b) and 6, regrowth over the aperture edges results in a large number of crystal defects at the inclined sidewalls, such as stacking faults and threading dislocations. On the other hand, no defects or non-idealities are observed at the regrowth interface along the entire current aperture, and neither above nor below the planar parts of the blocking layers. The defects are thus limited to the vicinity of the inclined sidewalls, constituting $<1\%$ of the aperture width. High-resolution TEM (HRTEM) imaging is used to take a closer look at the aperture edge in figure 6(a) and reveal the origin of the observed defects. Whereas a perfect AlGaAs crystal structure grows above the planar surface of the blocking layers, lateral growth takes place over the inclined sidewall. This lateral growth in free space without a lattice-matched buffer at the bottom results in the formation of a large number of stacking faults and twins, as shown in figures 6(c) and (d). Similar defect formation takes place at the bottom of the aperture edge (figure 6(b)), where the material growing over the bottom of the aperture coalesces with the material nucleating on the sidewall. The dark regions frequently observed at the inclined sidewalls (figure 6(a)) are attributed to the formation of voids containing amorphous material, as shown in figure 6(d). The void formation was confirmed using EDXS, which could not precisely identify the material composition, but detected low-intensity oxygen peaks. One possible interpretation of the EDXS analysis is that the amorphous material in the voids is Al_2O_3, which has significantly lower refractive index ($n \approx 1.7$) than the surrounding layers. To estimate the potential influence of the voids on lateral waveguiding, we repeat the QIP2

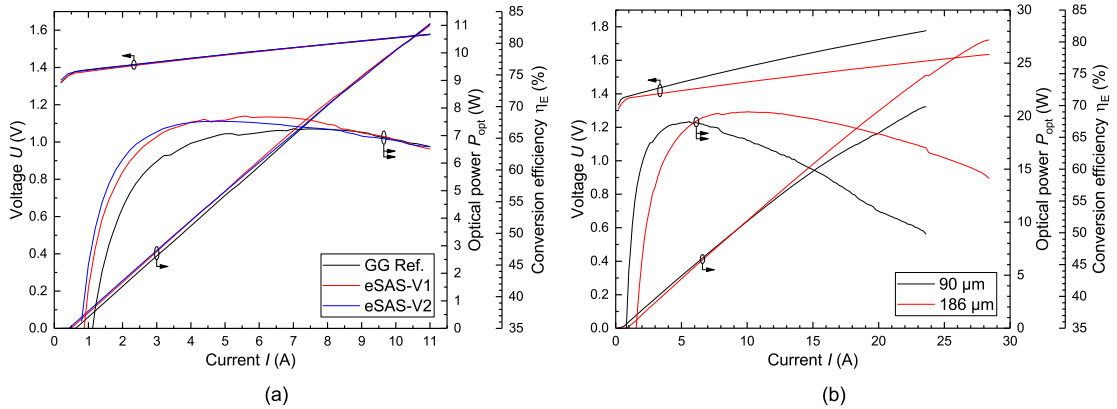

Figure 7. Voltage, optical power and conversion efficiency as functions of current under CW operation at 25 °C for the following devices ($L = 4$ mm): (a) eSAS-V2, eSAS-V1 and gain-guided reference SEs with $W = 90$ μm, and (b) eSAS-V2 SEs with $W = 90$ and 186 μm, measured up to high current levels.

simulation (see section 2), modelling the void as a 15 nm Al_2O_3 layer replacing part of the thicker GaAs layer in the outer blocking region. With these assumptions, $\Delta n_{\mathrm{eff},0}$ is reduced from -1.85×10^{-3} to -1.05×10^{-3}, indicating that the voids can potentially induce index guiding, but the anti-guiding of the current-blocking layers would likely remain the dominant waveguiding mechanism. The defects at the aperture edges (stacking faults, twins and voids) have had to date no observed negative impact on device performance, as discussed in section 4. To limit or eliminate defects in future realizations, regrowth parameters have to be optimized in order to control growth kinetics and thus lateral and vertical growth rates.

4. Measurement results and analysis

After ensuring that the eSAS-V2 design has been successfully realized, we proceed to process, mount and characterize devices, following methods described in [17] and summarized here for convenience. First, the wafers are cleaved into bars, whose front and rear facets are then passivated with zinc selenide and coated with dielectric layers to have reflectivities of 1% and 98%, respectively. After that, the bars are cleaved into single-emitters (SEs) with resonator length $L = 4$ mm and varying stripe widths $W = 20$, 50, 90 and 186 μm, which are then mounted p-side down on expansion-matched copper-tungsten (CuW) submounts. For testing, the CuW submounts are mounted on a gold-plated copper heat sink to enhance heat dissipation, with the resulting R_{th} typically in the 2–2.5 K/W range. Finally, the mounted SEs are characterized by measuring their power-voltage-current (PUI) characteristics and their beam quality (i.e. near- and far-field beam profiles) under continuous-wave (CW) operation at 25 °C. For the PUI measurement, optical power is measured using a calibrated thermoelectric detector and voltage is measured using a four-terminal configuration, while for the beam quality measurement, the beam profiles are imaged onto a moving slit using a telescopic arrangement. For comparison, eSAS-V1 SEs with the same dimensions are also mounted and characterized, as well as reference gain-guided (GG) SEs, which are processed on the same wafers with eSAS devices by completely etching the blocking layers between the two growth steps and defining W using selective shallow ion implantation of the p^+-contact layer (see figure 1). In the following, we present the SE measurement results of the three lateral design variants and compare them.

In figure 7(a), PUI characteristics of a representative SE of each design variant with $W = 90$ μm are shown, measured up to 11 A, and their electro-optical performance metrics are extracted. As expected from simulation (see figure 3), eSAS-V2 exhibits the lowest I_{th} (427 mA), followed by eSAS-V1 (489 mA), and finally the GG reference (598 mA). All three variants exhibit very similar slopes of the P-I curve. They also have very similar U-I characteristics, indicating no significant increase in series resistance resulting from the current confinement. In terms of $\eta_{\mathrm{E,peak}}$, eSAS-V2 (67.7%) shows a clear advantage over the GG reference (66.5%), but the highest value is achieved by the eSAS-V1 SE (68.7%). However, at $P_{\mathrm{opt}} = 10$ W, it is clear that the three variants exhibit very similar η_{E}, with values in the 64.5–65.0% range.

Figure 7(b) shows the PUI characteristics of two representative eSAS-V2 SEs ($W = 90$ & 186 μm, $L = 4$ mm), measured up to high currents to test their power saturation and thermal roll-over behavior. We observe that the 90 μm SE does not fail up to a current of 23.6 A, corresponding to $P_{\mathrm{opt}} = 20.9$ W, with $\eta_{\mathrm{E}} = 51.5\%$ at 20 W. Similarly, the 186 μm SE does not fail up to a current of 28.4 A, corresponding to $P_{\mathrm{opt}} = 27.2$ W, with $\eta_{\mathrm{E}} = 69.0\%$ at its peak, 65.8% at 20 W, and 61.6% at 25 W. These results clearly demonstrate

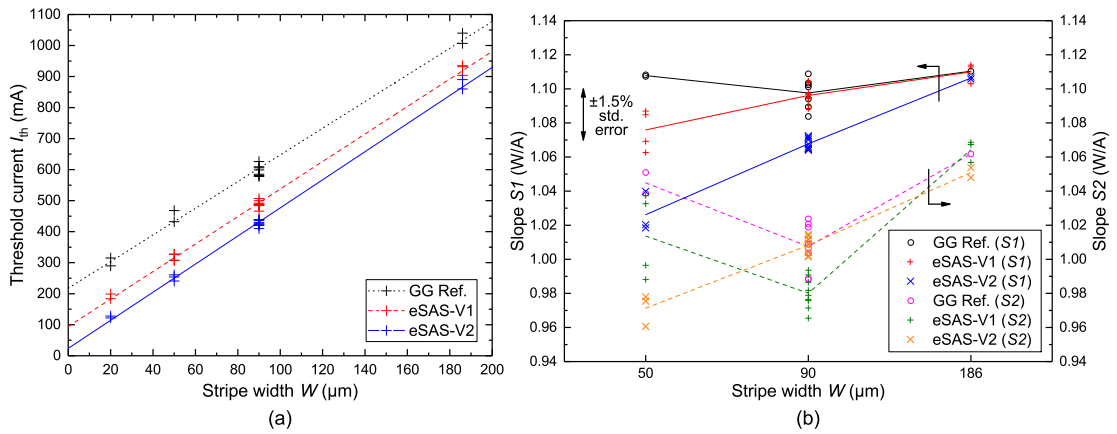

Figure 8. (a) Threshold current I_{th} as a function of stripe width W under CW operation at 25 °C for ⩾13 SEs of each design variant: gain-guided reference, eSAS-V1 and eSAS-V2, and (b) slopes $S1$ and $S2$ for the SEs with $W = 50$, 90 and 186 μm.

the benefits of the ETAS vertical structure used in this realization, which enables high η_E at high P_{opt} (see section 2). The high P_{opt} levels obtained by the SEs also show that despite the defects observed using TEM (see section 3.3), the eSAS-V2 configuration does not cause early power saturation or failure. However, aging tests are still necessary to ensure that it does not negatively affect device reliability and lifetime.

PUI measurements are carried out for a large number of SEs (⩾13 of each variant) with varying W, and the extracted performance metrics are analyzed to obtain reliable trends. For example, I_{th} values can be used to quantify and compare the effectiveness of the eSAS variants in reducing current loss outside the BAL stripe due to current spreading [6, 10]. As shown in figure 8(a), the I_{th} values are plotted as a function of W for each variant, and linear fits are extrapolated to intercept with the $W = 0$ axis. The intercept points ($I_{th,0}$) are empirical estimates of the spreading current lost in the device edges in each case. It is clear from the figure that as expected, the gain-guided reference exhibits the highest $I_{th,0}$ (218 mA), followed by eSAS-V1 (94 mA), and finally eSAS-V2 (24 mA). These values correspond to a current loss reduction of 89% for V2 and 57% for V1 relative to the reference, which are close to the estimates from the analytic simulation model (85.5% and 65.5% respectively; see section 2).

In another example shown in figure 8(b), the extracted slope values $S1$ and $S2$ of the SEs with varying W are plotted for each variant, where $S1$ represents the slope of the first half of the P-I curve between I_{th} and the maximum operating current (i.e. at lower current levels), while $S2$ represents the slope of the second half (i.e. at higher current levels). We limit the comparison here to SEs with $W = 50$, 90 and 186 μm, measured up to 7, 11 and 15 A, respectively. We observe that slope values $S1$ and $S2$ tend to be similar for all variants, with differences roughly lying within the ±1.5% standard error margin [27] as previously reported in [10], with the exception of 50 μm eSAS-V2 SEs whose slope is significantly lower than their counterparts. In any case, the results indicate that the expected slope enhancement [4, 10] could not be demonstrated so far from either eSAS variant, even though edge leakage is almost completely suppressed. One possible explanation is LCA occuring not at the stripe edges, but rather within the stripe at the front facet, which can be explained by lateral spatial hole burning and thermal lensing in the presence of longitudinal temperature variation. This can result in non-ideal overlap between the lateral carrier and optical profiles and therefore lower gain [28, 29].

Next, we proceed to beam quality characterization. Figure 9 shows the near- and far-field intensity profiles and the corresponding beam parameters $W_{95\%}$ and $\theta_{95\%}$ for an exemplary SE of each lateral design variant with $W = 90$ μm at different operating points ($P_{opt} = 2.5$, 5, 7.5 and 10 W). Significant narrowing of the near-field is observed in both eSAS variants compared to the reference over the whole P_{opt} range, due to the reduced LCA. The eSAS-V1 SE follows roughly the same trend as the gain-guided reference, with a wide $W_{95\%}$ at lower P_{opt} levels that is strongly narrowed at the highest operating point due to thermal lensing. Conversely, the eSAS-V2 SE exhibits a different tendency, with a constant, narrow $W_{95\%}$ over the whole P_{opt} range, which is consistent with the presence of index guiding [17]. In addition, the near-field profiles of the eSAS-V2 SE show weaker lateral intensity modulation (i.e. less pronounced peaks) compared to the other variants, which is also consistent with index guiding [30]. The obtained $W_{95\%}$ values at $P_{opt} = 10$ W correspond to a narrowing of 13.2% for V2 and 15.4% for V1 relative to the reference. In terms of far field, the reference and V1 SEs have similar $\theta_{95\%}$ values and no obvious trend in the profiles over the whole P_{opt} range, which is in agreement with previous results [10, 11]. On the other hand, the V2 SE has a significantly wider $\theta_{95\%}$ at all P_{opt} levels, which can also be explained by index guiding. Overall, at $P_{opt} = 10$ W, the eSAS-V2 SE has $BPP_{lat} = 3.30$ mm·mrad, compared to 3.06 mm·mrad for the eSAS-V1 SE and 3.47 mm·mrad for the reference. These correspond to B_{lat} values of 3.03,

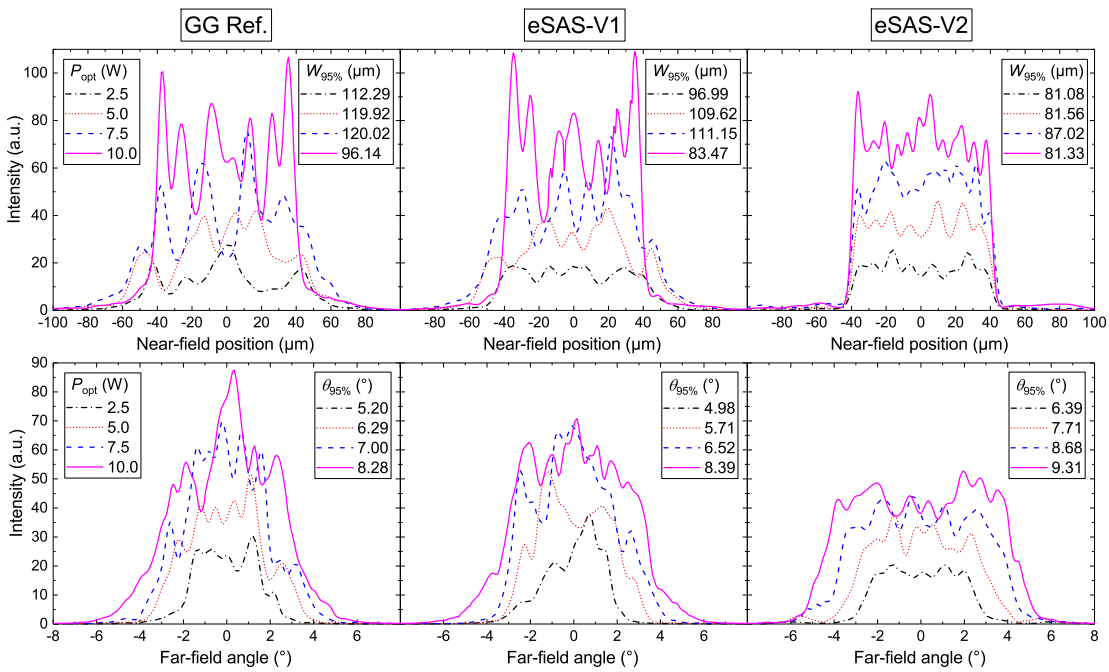

Figure 9. Measured optical intensity as a function of near-field position (top) and far-field angle (bottom) under CW operation at 25 °C and different P_{opt} levels for a representative SE ($W = 90$ μm, $L = 4$ mm) of each design variant: gain-guided reference (left), eSAS-V1 (center), and eSAS-V2 (right). The corresponding beam parameters $W_{95\%}$ and $\theta_{95\%}$ are indicated in the legends.

3.27 and 2.88 W/(mm·mrad), respectively. Both eSAS variants have thus demonstrated improved beam quality compared to the reference, but despite stronger suppression of LCA at stripe edges, the improvement shown by the V2 variant (5.2%) is not as large as that shown by the V1 variant (13.5%), likely due to index guiding.

To obtain reliable trends, near-field and far-field profiles are measured for a large number of SEs ($\geqslant$7 of each variant) with $W = 90$ μm at the 4 operating points mentioned above, and are used to extract $W_{95\%}$ and $\theta_{95\%}$ and subsequently calculate BPP_{lat}. As shown in figure 10, these parameters are then plotted as functions of the active zone temperature increase, calculated as $\Delta T_{AZ} = R_{th} \cdot (I \cdot U - P_{opt})$. In terms of the near field (figure 10(a)), the observed trends confirm the findings from the individual SE results (see above). We additionally note that in V2 SEs, as well as in V1 SEs at the highest operating point ($P_{opt} = 10$ W, $\Delta T_{AZ} = 12 \pm 1$ K), $W_{95\%}$ is significantly smaller than $W = 90$ μm. This is consistent with strong longitudinal-lateral temperature variation [28], but it is unclear why this would occur at low ΔT_{AZ} levels in V2 SEs, so this remains a topic for further investigation. The near-field behavior observed in eSAS-V2 SEs, namely narrow and roughly constant $W_{95\%}$ with increasing P_{opt} and heat levels, can be exploited using SEs with large stripe widths for efficient coupling into optical fibers. The far field trends (figure 10(b)) are also in agreement with the individual SE findings (see above). However, we observe that while $\theta_{95\%}$ is generally wider in V2 SEs, it becomes more comparable to V1 and reference values at the highest operating point. This may be evidence that as thermal lensing becomes stronger, it counteracts the built-in index anti-guiding as estimated in section 2, resulting in improved beam quality, but further studies are also necessary to confirm this.

The resulting BPP_{lat} values, plotted in figure 10(c), directly demonstrate the improvement in beam quality by using eSAS. We observe that V1 SEs tend to have the lowest (best) values over the whole ΔT_{AZ} range. V2 SEs also tend to exhibit lower values than gain-guided reference SEs, especially at higher operating points, despite their wider $\theta_{95\%}$. Following [8, 12], we obtain further insight on the beam quality enhancement by applying linear fits to the BPP_{lat} values and using the simple empirical model $BPP_{lat} = BPP_0 + S_{th} \cdot \Delta T_{AZ}$. In this model, the intercept term BPP_0 represents a background level, regulated by non-thermal contributions such as process- or packaging-induced waveguiding, while the slope term S_{th} represents the impact of heat- and bias-dependent mechanisms. We observe that while BPP_0 is consistent in all three variants (2 ± 0.05 mm·mrad), S_{th} is reduced from 0.149 mm·mrad/K for the reference design to 0.124 for eSAS-V2 (17% reduction) and 0.108 for eSAS-V1 (28% reduction). The S_{th} reduction results from the suppression of LCA, which is not directly a thermal mechanism, but is nonetheless dependent on bias current through the increasing carrier density at the stripe edges, which allows higher order modes to reach threshold and be guided by the existing thermal lens [7, 8, 12]. This result is consistent with [8], where a comparable S_{th} reduction was shown using deep ion implantation through the active zone, at the cost of significantly reduced P_{opt} and η_E. Using eSAS, we have demonstrated here a significant reduction of S_{th} and BPP_{lat} with no efficiency penalty.

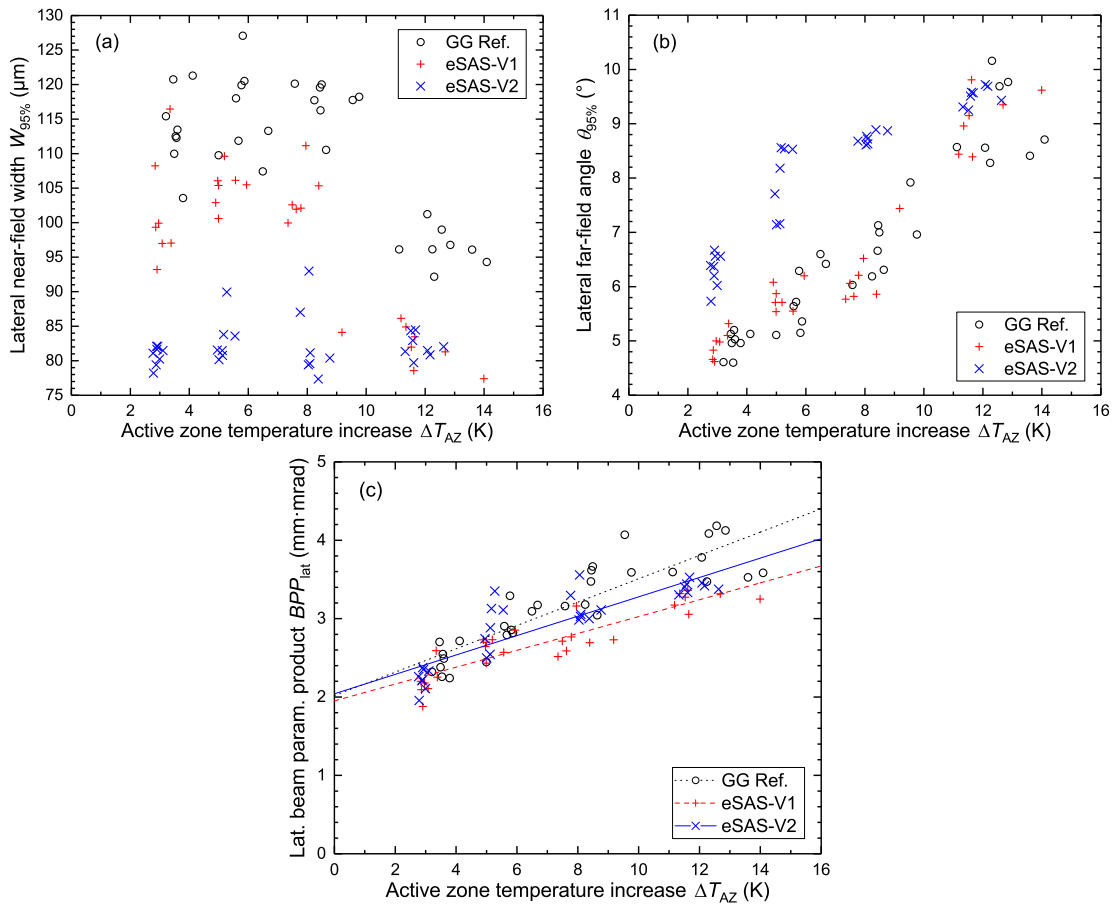

Figure 10. (a) Measured lateral near-field width $W_{95\%}$, (b) far-field angle $\theta_{95\%}$ (both with 95% power content) and (c) beam parameter product BPP_{lat}, as functions of active zone temperature increase ΔT_{AZ} for ⩾7 SEs of each design variant: gain-guided reference, eSAS-V1, and eSAS-V2, all having $W = 90$ μm and $L = 4$ mm and tested under the same conditions and P_{opt} levels as in figure 9.

5. Summary and conclusion

In this work, we have presented high-power GaAs-based broad-area diode lasers with a novel variant of the enhanced self-aligned lateral structure (eSAS), where a two-step epitaxial growth process with an added *in situ* etching step enables the realization of laterally-structured n-doped current-blocking layers within the p-$Al_{0.8}GaAs$ cladding layer of an extreme-triple-asymmetric epitaxial structure with a thin p-side waveguide. With this new configuration (eSAS-V2), the blocking layers are located much closer to the active zone (200–300 nm offset) compared to the previous eSAS-V1 variant (800–900 nm), leading to stronger current and carrier confinement under the central stripe, targeting better suppression of current spreading and lateral carrier accumulation (LCA). In addition to their deeper position within the vertical structure, the blocking layers are optimized for tunnel current suppression by introducing a thin undoped layer on each side, resulting in a p-i-n-i-p configuration. This configuration has shown improved current-blocking capability, limiting current density to 9 orders of magnitude lower than threshold within the typical diode laser operating voltage range. In the first successful realization of the eSAS-V2 design, *in situ* etching enabled the regrowth of the $Al_{0.8}GaAs$ cladding with very low oxygen incorportation. Some defects were created at the sidewalls of the etched stripe, but the central current path under the stripe was defect-free. eSAS-V2 single-emitters (SEs) with varying stripe widths and 4 mm resonator length are processed and mounted, and their performance under continuous-wave operation is contrasted with comparable eSAS-V1 and gain-guided reference SEs. eSAS-V2 SEs show a strongly reduced threshold current for all stripe widths, corresponding to an estimated 89% reduction of current loss in device edges, indicating near total suppression of lateral current spreading. Series resistance remains roughly constant in all three variants, with no increase due to current confinement. Slope of the power-current curve is also found to be broadly consistent, meaning that the slope enhancement expected from reducing current spreading could not be demonstrated. Nonetheless, the threshold reduction in both eSAS variants enables improved peak conversion efficiency, reaching up to 69%. In addition, eSAS-V2 SEs are operated up to high current levels and are shown to maintain high conversion efficiency (51.5% at 20 W for a 90 μm SE), indicating that the defects at the stripe edges do not cause early power saturation or failure. In terms of beam quality, both eSAS variants

exhibit significantly narrower near-field width than reference SEs due to reduced LCA, leading to a smaller beam parameter product. However, unlike eSAS-V1 and reference SEs, eSAS-V2 SEs exhibit a roughly constant near-field width with almost no dependence on optical power or heat level. Their near-field profiles also show weaker lateral intensity modulation, and their far-field angles are broader than the other variants. These findings are consistent with the introduction of additional lateral index guiding in this first realization of the eSAS-V2 configuration. Improved beam quality is nonetheless demonstrated in comparison to gain guiding, but suppressing this additional index guiding will allow further improvement and higher brightness to be achieved. An overall best eSAS lateral brightness of 3.27 W/(mm·mrad) for a 90 μm SE is achieved, 13.5% higher than the gain-guided reference.

Acknowledgments

We would like to thank G Tränkle, P Ressel, O Krüger and S Knigge for supporting this work, and TRUMPF Laser GmbH for funding it.

Data availability statement

All data that support the findings of this study are included within the article (and any supplementary files).

ORCID iDs

M Elattar https://orcid.org/0000-0003-0822-0297
P Della Casa https://orcid.org/0000-0001-8393-4498
P Crump https://orcid.org/0000-0001-6723-8863

References

[1] Crump P *et al* 2012 *Semicond. Sci. Technol.* **27** 045001
[2] Piprek J 2013 *Proc. SPIE* **8619** 861910
[3] Kaul T *et al* 2019 *IEEE J. Sel. Top. Quantum Electron.* **25** 1501910
[4] Smowton P M and Blood P 1997 *IEEE J. Sel. Top. Quantum Electron.* **3** 491–8
[5] Crump P *et al* 2008 *Appl. Phys. Lett.* **92** 131113
[6] Wenzel H *et al* 2000 *Semicond. Sci. Technol.* **15** 557–60
[7] Piprek J and Simon Li Z M 2013 *Appl. Phys. Lett.* **102** 221110
[8] Winterfeldt M *et al* 2015 *IEEE Photonics Technol. Lett.* **27** 1809–12
[9] Zeghuzi A *et al* 2019 *IEEE J. Quantum Electron.* **55** 2000207
[10] Elattar M *et al* 2020 *Semicond. Sci. Technol.* **35** 095011
[11] Elattar M *et al* 2021 *Proc. SPIE* **11705** 117050N
[12] Crump P *et al* 2022 *IEEE J. Sel. Top. Quantum Electron.* **28** 1501111
[13] Groom K M *et al* 2008 *Electron. Lett.* **44** 905–6
[14] Yamagata Y *et al* 2015 *Proc. SPIE* **9348** 93480F
[15] Yamagata Y *et al* 2020 *Proc. SPIE* **11262** 1126203
[16] Kaul T *et al* 2018 *Proc. SPIE* **10514** 105140A
[17] Winterfeldt M *et al* 2014 *J. Appl. Phys.* **116** 063103
[18] Wenzel H and Wünsche H-J 1990 *Phys. Status Solidi* **120** 661–73
[19] Schultz C M *et al* 2012 *Appl. Phys. Lett.* **100** 201115
[20] Fair R B and Wivell H W 1976 *IEEE Trans. Electron. Devices* **23** 512–8
[21] Ahmed K, Elahi M M M and Islam M S 2012 *Proc. Int. Conf. Informat., Electron. & Vis. (ICIEV)* pp 521–4
[22] Bawamia A I *et al* 2009 *Appl. Phys.* B **97** 95–101
[23] Zeghuzi A *et al* 2019 *IEEE J. Sel. Top. Quantum Electron.* **25** 1502310
[24] Yonezu H *et al* 1973 *Jpn. J. Appl. Phys.* **12** 1585–92
[25] Tsang W T 1978 *J. Appl. Phys.* **49** 1031–44
[26] Bugge F *et al* 2011 *J. Cryst. Growth* **315** 74–7
[27] Crump P *et al* 2013 *IEEE J. Sel. Top. Quantum Electron.* **19** 1501211
[28] Rauch S *et al* 2017 *Appl. Phys. Lett.* **110** 263504
[29] Arslan S *et al* 2022 *Proc. SPIE* **12021** 120210F
[30] Koester J-P *et al* 2020 *Proc. SPIE* **11274** 112740I